

Journal of Materials Chemistry A

Accepted Manuscript



This is an *Accepted Manuscript*, which has been through the Royal Society of Chemistry peer review process and has been accepted for publication.

Accepted Manuscripts are published online shortly after acceptance, before technical editing, formatting and proof reading. Using this free service, authors can make their results available to the community, in citable form, before we publish the edited article. We will replace this *Accepted Manuscript* with the edited and formatted *Advance Article* as soon as it is available.

You can find more information about *Accepted Manuscripts* in the [Information for Authors](#).

Please note that technical editing may introduce minor changes to the text and/or graphics, which may alter content. The journal's standard [Terms & Conditions](#) and the [Ethical guidelines](#) still apply. In no event shall the Royal Society of Chemistry be held responsible for any errors or omissions in this *Accepted Manuscript* or any consequences arising from the use of any information it contains.

Photoelectrochemical water splitting at low applied potential using NiOOH coated codoped (Sn, Zr) α -Fe₂O₃ photoanode

Andebet Gedamu Tamirat^a, Wei-Nien Su^{*b}, Amare Aregahegn Dubale^a, Hung-Ming Chen^a, and Bing-Joe Hwang^{*ac}

^aNanoElectrochemistry Laboratory, Department of Chemical Engineering, National Taiwan University of Science and Technology, Taipei, 106, Taiwan. E-mail: bjh@mail.ntust.edu.tw; Fax: +886-2-27376644

^bNanoElectrochemistry Laboratory, Graduate Institute of Applied Science and Technology, National Taiwan University of Science and Technology, Taipei 106, Taiwan

^cNational Synchrotron Radiation Research Center, Hsinchu, 30076, Taiwan

Abstract: One of the major challenges in photoelectrochemical water splitting is to develop an efficient photoanode that can oxidize water at low applied potential. Herein, a codoped (Sn, Zr) α -Fe₂O₃ photoanode modified with stable and earth abundant nickel oxyhydroxide (NiOOH) co-catalyst that can split water at low applied potential is reported. First, unintentional gradient monodoped (Sn) α -Fe₂O₃ photoanode was synthesized at controlled annealing temperature that achieved a photocurrent density of 0.86 mA cm⁻² at 1.23 V vs. RHE. Further doping with optimized amount of Zr outperformed the monodoped (Sn) α -Fe₂O₃ photoanode providing significantly much higher photocurrent density (1.34 mA cm⁻²). The remarkably improved electrical conductivity and more than three times higher charge carrier density (as evidenced from electrochemical impedance spectroscopy measurements and Mott-Schottky analysis) of the codoped (Sn, Zr) α -Fe₂O₃ photoanode highlights the importance of codoping. The synergetic effect of codoping (Sn, Zr) led to 1.6 fold enhancement in charge separation efficiency at 1.23 V than that of the monodoped (Sn) α -Fe₂O₃ photoanode. The NiOOH modified codoped (Sn, Zr) α -Fe₂O₃ photoanode exhibited drastically lower onset potential (0.58 V) and a photocurrent density of 1.64 mA cm⁻² at 1.23 V. Interestingly a 160 mV cathodic shift in photocurrent onset potential was also observed. Concomitant with this, the NiOOH modified codoped (Sn, Zr) α -Fe₂O₃ photoanode exhibited 1.6 to 9.5 fold enhancement in charge injection efficiency (η_{inj}) at kinetic control region of 0.7 to 0.9 V compared to unmodified codoped photoanode. Gas

evolution measurements also showed that the NiOOH modified codoped α -Fe₂O₃ photoanode achieved an average Faradaic efficiency of 93%.

Keywords: Photoelectrochemical water splitting, codoped (Sn, Zr) α -Fe₂O₃ photoanode, nickel oxyhydroxide, charge separation efficiency, charge injection efficiency

1. Introduction

Due to the growing demand for energy supplies, the depletion of fossil fuels and global warming much effort has been put forth in searching for clean and renewable energy sources. Solar energy is among the most promising candidates to serve as an energy source at the lowest cost of environment. However, the intermittence of solar light hampers its direct use in many applications. To better utilize the solar energy, technologies that can efficiently and inexpensively store solar energy for off-hour use are needed. Photoelectrochemical (PEC) water splitting using semiconductor electrodes is a promising approach to alleviate this energy challenge. The development of semiconductor electrodes for PEC water splitting, which must satisfy a number of requirements and capable of performing reactions at high efficiencies, is therefore of paramount importance. Among various water splitting photoanode materials, hematite (α -Fe₂O₃, α is omitted henceforth) has several promising properties, including smaller band gap (1.9 ~ 2.2 eV) that maximizes absorption of the solar spectrum,¹ stability in aqueous environment under typical operating conditions,² abundance,³ and affordability.⁴ All these properties make it a potential candidate as a water splitting photoanode for the main proof-of-concept demonstrations. However, several key issues such as relatively poor absorption coefficient (due to an indirect band gap),^{3, 5} very short excited-state lifetime ($\sim 10^{-12}$ s),³ poor oxygen evolution reaction kinetics,^{1, 3} and a short hole diffusion length (2-4 nm)^{1, 6} limit its PEC activity.

Even though tremendous efforts have been made to improve the photocatalytic activity of Fe₂O₃, the actual water oxidation photocurrent is still by far lower than the maximum theoretical water oxidation photocurrent (J_{\max}) that reaches 12.5 mA cm⁻² under AM 1.5 G solar illumination. There are three basic governing factors which make the practical water oxidation photocurrent ($J_{\text{H}_2\text{O}}$) much lower. These include; limited photon absorption, poor charge separation efficiency (η_{sep}), and low charge injection efficiency (η_{inj}).⁷⁻⁹ So far, various efforts have been devoted to

overcome these constraints and improve the PEC performance of hematite. The photon absorption property can be enhanced by nanostructuring,¹⁰ using more than one absorber (heterostructures),¹¹ using localized surface plasmons,¹² quantum dot sensitization¹³ etc. Introduction of metallic and nonmetallic dopants is another possible strategy to increase photon absorption through band gap narrowing.¹⁴ Many attempts have also been made to enhance the poor charge separation efficiency of Fe₂O₃. These include reduction of film thickness, aiming to improve the hole diffusion length of hematite.⁶ Doping with mono-atomic ions of charge greater than +3 will introduce additional majority carriers and create steeper voltage gradients (thinner space-charge layers) that enhances charge separation.¹⁴ Formation of heterojunctions,¹¹ graphene composites,^{15, 16} introducing electron collecting scaffolds¹⁷ are other alternative approaches to enhance charge separation efficiency. Poor charge injection efficiency can be improved either by lowering potential-dependent rate constants for surface-mediated charge recombination or by increasing the rate constant for hole transfer from the photoelectrode to molecular reactants.¹⁴ The former can be overcome by passivating surface localized electron trap states by thin over layer coatings. The later is more challenging, as it is difficult to see how hematite itself could be induced to transfer photogenerated holes more rapidly. An alternative and more efficient approach would be to coat Fe₂O₃ with efficient co-catalysts which are capable of transferring holes to H₂O or OH⁻ much more quickly and reduce the water oxidation over-potential.

In the present study, we synthesized single-crystalline 1-D Fe₂O₃ nanorod arrays formed by in-situ two step controlled annealing (at 500 and 800 °C) of 1-D β-FeOOH nanorod arrays grown directly on fluorine doped tin oxide (FTO) coated glass substrate via a simple solution-based method. Moreover, we examined the effect of unintentional gradient Sn doping caused by high temperature annealing on the PEC performance of Fe₂O₃. The diffusion of Sn from the FTO layer to Fe₂O₃ bulk by high temperature calcination has been reported previously.^{1, 18, 19} However, none of these studies have mentioned the gradient doping property of Sn. In addition to gradient Sn doping, we employed optimum amount of Zr dopant to introduce additional majority carriers and improve the electrical conductivity of the electrode further. Few recent studies have showed that Zr-doped hematite photoanode exhibited a significantly improved PEC response.^{20, 21} These findings are also supported by ab initio quantum mechanics calculation recently done by Liao et al.²² The authors suggested that zirconium doping is superior to titanium doping; the most widely

studied dopant on hematite; because the former dopant do not act as electron trapping sites due to the higher instability of Zr (III) compared to Ti (III).

After enhancing the charge separation efficiency via doping, our next goal is to overcome the large water-splitting overpotential of hematite which is caused by its poor oxygen evolution reaction (OER) kinetics. Hence the next step is to develop a low-cost and high-efficiency OER catalyst which can able to oxidize water at low applied potential. Recently, Ni based oxygen evolution catalysts have attracted a lot of interest, due to their high catalytic performance, low cost and low toxicity.^{2, 23, 24} More recently, there have been some promising studies showing NiOOH based oxygen evolution catalysts (OEC) as a robust, high catalytic activity and even more active than RuO₂, a well-established catalyst for the OER.^{9, 25} However, to date no study has been conducted on NiOOH OEC for improving the water oxidation kinetics of Fe₂O₃ electrode. Herein, we report the study of the catalytic effect of NiOOH on codoped (Sn, Zr) Fe₂O₃ photoanode for photoelectrochemical water oxidation. We employed photoassisted electrodeposition technique which helps to deposit more uniform and compact NiOOH layer with lower loading amount. The charge separation and injection properties were examined in the presence of 0.5 M hydrogen peroxide (H₂O₂), which served as the hole scavenger. Because the oxidation of H₂O₂ is thermodynamically and kinetically more facile than oxidation of water, therefore, measuring photocurrent for H₂O₂ oxidation enables investigation of the PEC properties of Fe₂O₃ independently of its poor water oxidation kinetics. PEC transient photocurrent measurements, Mott-Schottky and impedance analyses were also employed to further understand the dynamics of photogenerated carriers.

2. Experimental Section

2.1. Materials and chemicals

Iron (III) chloride hexahydrate (99+%, Acros Organics), nickel (II) sulfate hexahydrate (99%, Acros Organics), zirconium (IV) chloride (98%, Acros Organics), hydrogen peroxide (34.5-36.5%, Sigma Aldrich), isopropyl alcohol (99.5% min., Mallinckrodt Chemicals), ethanol (99.5%, Shimakyu's Pure Chemicals), sodium hydroxide (99%, Shimakyu's pure chemicals). All reagents were used directly without any further purification.

2.2. Synthesis of samples

2.2.1. Preparation of codoped (Sn, Zr) Fe₂O₃ nanorod arrays

The hematite photoanodes were prepared via a simple solution-based method followed by in-situ two-step annealing. First, an aqueous solution containing 0.15 M iron (III) chloride hexahydrate and 0.15 M urea was prepared. In the meantime, a piece of FTO glass was cleaned ultrasonically with EXTRAN MA 02 neutral liquid detergent and washed with DI water and isopropyl alcohol followed by excess DI water. Then the clean FTO glass was put into a Teflon-lined stainless steel autoclave facing its conductive side towards the wall of the Teflon. 10 mL precursor solution was added to the autoclave then sealed and heated at 100 °C for 10 hours. Next, the autoclave was cooled down naturally, and the film coated FTO glass was taken out of the Teflon, washed with absolute ethanol and DI water separately then air dried. A uniform yellow layer of FeOOH film was coated on the FTO glass. The FeOOH film was changed to Fe₂O₃ via in-situ two-step annealing, initially at 500 °C for 2 h followed by 20 min short annealing time at 800 °C. The second annealing stage is responsible for enhancing crystallinity and diffusion of tin from the FTO substrate to hematite bulk resulting in gradient tin doped hematite (Sn-Fe₂O₃). For zirconium doped samples, various amount of zirconium (IV) chloride was added into the precursor solution as a dopant source. ZrCl₄ was used as the zirconium source because it doesn't introduce other impurity anion. Moreover, hydrolysis of ZrCl₄ was inhibited due to a low concentration of Zr⁴⁺ and low pH of the solution, which is very important for doping.

2.2.2. Photo-assisted electrodeposition of NiOOH catalyst

For photo-assisted electrodeposition of NiOOH catalyst the codoped (Sn, Zr) Fe₂O₃ electrode was transferred to a three-electrode PEC cell containing 0.1 M nickel (II) sulfate solution, its pH is adjusted to 7. The Fe₂O₃ electrode was used as working electrode, the Ag/AgCl electrode was used as reference electrode and Pt mesh was used as the counter electrode. Prior to the deposition, the solution was purged with nitrogen gas for 30 min. During deposition, the Ni²⁺ solution was kept at 45 °C and continuously stirred using a magnetic stirrer. The light was back-side illuminated. During illumination, the holes generated in the valence band of Fe₂O₃ are used to oxidize Ni²⁺ ions to Ni³⁺ ions, which precipitate as NiOOH on the surface of the Fe₂O₃ electrode ($\text{Ni}^{2+}(\text{aq}) + \text{h}^+ + 3\text{OH}^- \rightarrow \text{NiOOH}(\text{s}) + \text{H}_2\text{O}$). To facilitate the deposition, an external bias of 0.2 V vs. Ag/AgCl was applied. The thickness of the NiOOH layer was controlled by varying the

amount of charge that passes during the deposition. Various deposition charges (*i.e.*, 20, 35, 50, 75, and 100 mC cm⁻²) were conducted and the photoanode with ~50 mC cm⁻² deposition showed the highest photocurrent. For comparison NiOOH was electrodeposited for 3 min by applying 1.2 V vs. Ag/AgCl. After deposition, the electrode was thoroughly rinsed with DI water and air dried.

2.3. Structural characterization

The crystalline phase of the samples was identified by D2 phaser XRD-300W diffractometer equipped with Cu K α ($\lambda = 1.5406 \text{ \AA}$) radiation source operating at 30 kV and 10 mA. The morphology of the samples was examined by field-emission scanning electron microscopy (JSM 6500F, JEOL) coupled with energy-dispersive X-ray analysis (EDX) with an accelerating voltage of 15 kV. A dual-beam focused ion beam (FIB, FEI Quanta3D FEG) was used for cross-sectional sample cutting using gallium ion sputtering. The FIB is equipped with scanning electron microscope (SEM) mode operated at an accelerating voltage of 30 kV to capture FIB images. Optical absorption measurements were performed using a JASCO (ISV-469) V 560 UV-visible spectrometer (UV-visible absorption spectrometer (Shimadzu, Model UV 3600)). X-ray photo-electron spectra (XPS) were also recorded at the National Synchrotron Radiation Research Centre (NSRRC), Taiwan with 24A XPS beam line station.

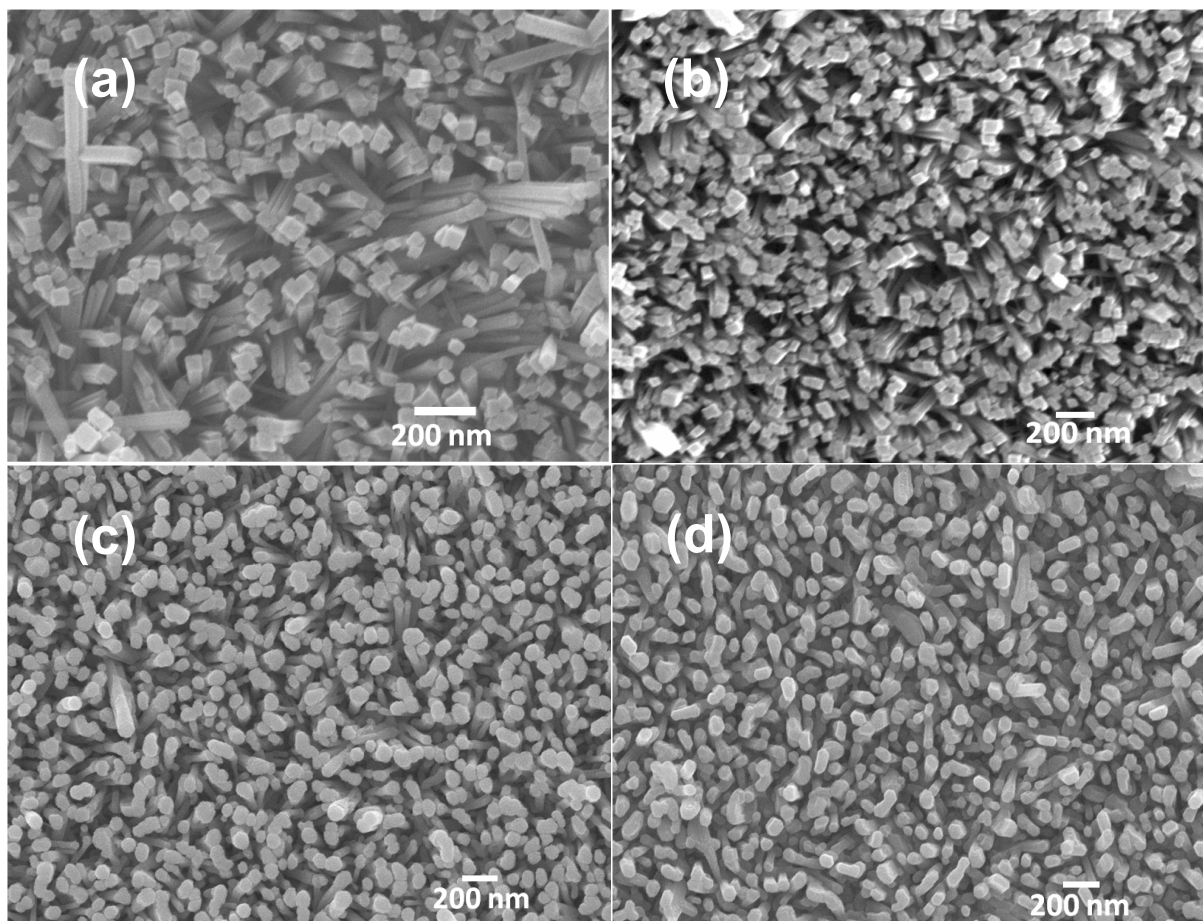
2.4. Photoelectrochemical measurements

The photocurrent measurements were conducted in a three electrode configuration with Ag/AgCl as a reference electrode, Pt wire as counter electrode, and the Fe₂O₃ photoanode as working electrode in 1 M NaOH (pH 13.6) electrolyte. A 300 W xenon arc lamp (6258, Newport) coupled with AM 1.5G filter was used as light source. Its intensity was calibrated at 100 mW cm⁻² (1 sun illumination) using silicon diode (Newport). All photoanodes were scanned from 0.4 to 1.8 V vs. RHE during the J–V analysis. From now on the potential is presented relative to the reversible hydrogen electrode (RHE) unless and otherwise stated. The electrochemical impedance spectroscopy (EIS) was performed using an electrochemical impedance analyzer with AC amplitude of 10 mV and frequency range between 100 kHz to 0.1 Hz. The measured EIS data were obtained at an applied bias of 0 V vs. RHE at 25 °C.

3. Results and Discussion

The morphological features of all samples were investigated by Field Emission scanning electron microscopy (FESEM). Figure 1(a) and (b) illustrate the SEM image of FeOOH nanorod films without and with Zr doping grown on FTO coated glass substrate. It is shown that, in both cases, the FeOOH nanorods are tetragonal in shape with sharp square cross-section at the top and have an average edge width of ~ 78 nm. It is confirmed that the size and shape of FeOOH film without and with Zr doping are the same, suggesting that Zr doping has no effect on the shape and morphology of FeOOH. Figure 1(c) depicts the SEM image of Zr doped FeOOH film after thermal treatment at 500 °C for 2 h. It is clearly shown that thermal treatment results remarkable effect on both the morphology and phase, changing square shaped FeOOH nanorods to round shaped Fe_2O_3 (confirmed by XRD). This morphological change is accompanied with increase in the average diameter of individual nanorods to ~ 82 nm. For PEC measurements, the Fe_2O_3 film was further annealed at 800 °C for 20 min (Figure 1(d)). The average diameter slightly increased to ~ 84 nm. However, we have found that high temperature annealing causes notable improvement in crystallinity. In addition, it causes diffusion of Sn from the FTO conducting substrate to the Fe_2O_3 bulk that leads to the formation of gradient doping. These two factors outweigh the undesirable increase in diameter of nanorods and led to enhanced photoelectrochemical performance. Diffusion of Sn from the FTO conductive substrate to the Fe_2O_3 film causes introduction of majority carriers and thereby enhances electrical conductivity. The photoanode is thus designated as codoped (Sn, Zr) Fe_2O_3 . Morrish et al. also studied the effects of the post-deposition annealing of Fe_2O_3 nanorods.¹⁹ They have found that high temperature annealing (750 °C) for a very short time (5 min) drastically improves the performance of Fe_2O_3 which was ascribed to the decrease in surface recombination due to lowering of surface trapping states and tin incorporation from the underlying FTO layer. Figure 1(e) demonstrates SEM image of the resulting codoped (Sn, Zr) Fe_2O_3 photoanode followed by photo-assisted electrodeposition of NiOOH. The current density during deposition was typically ~ 0.028 mA cm^{-2} , corresponding to the total charge of 50 mC cm^{-2} (Figure 2(a) and (b)). Because the valence band edge of Fe_2O_3 is located at ~ 2.5 V vs. NHE, the photogenerated holes have enough overpotential to oxidize Ni^{2+} to Ni^{3+} to produce the NiOOH catalyst on the Fe_2O_3 nanorod surface (Figure 2(c)). After 30 min deposition, thin NiOOH film was conformally

coated on the surface of Fe_2O_3 nanorods forming rough and wrinkled surface features. The entire body of individual Fe_2O_3 nanorods was uniformly covered by a rough layer of NiOOH . This is due to the fact that only Fe_2O_3 can photogenerate holes so that the catalyst can be deposited on the Fe_2O_3 surface selectively. For comparison, NiOOH cocatalyst was electrodeposited on codoped (Sn, Zr) Fe_2O_3 for 3 minutes at 1.2 V vs. Ag/AgCl (Figure 1(f)). A featureless dense layer was deposited on the entire electrode area including FTO surface. Unlike the photo-assisted electrodeposition, during simple electrodeposition the individual Fe_2O_3 nanorods were barely covered by NiOOH . In order to examine the film thickness, the sample has been cut with FIB using high energy Ga^+ ion beam. The cross-sectional image (Figure S1) shows that the average length of the nanorods reaches to ~ 700 nm representing the thickness of the film. The overall synthetic route is summarized and illustrated in Figure 2(d).



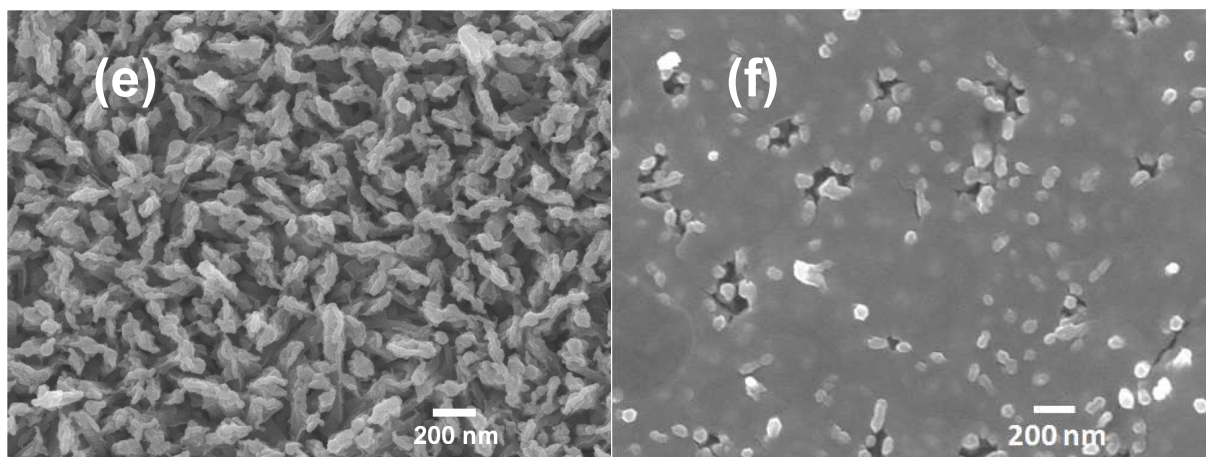


Figure 1. SEM images of (a) FeOOH without Zr doping, (b) FeOOH with Zr doping, (c) Zr doped Fe₂O₃ annealed at 500 °C, (d) codoped (Sn, Zr) Fe₂O₃ annealed at 800 °C, (e) codoped (Sn, Zr) Fe₂O₃ modified with photodeposited NiOOH, (f) codoped (Sn, Zr) Fe₂O₃ modified with electrodeposited NiOOH.

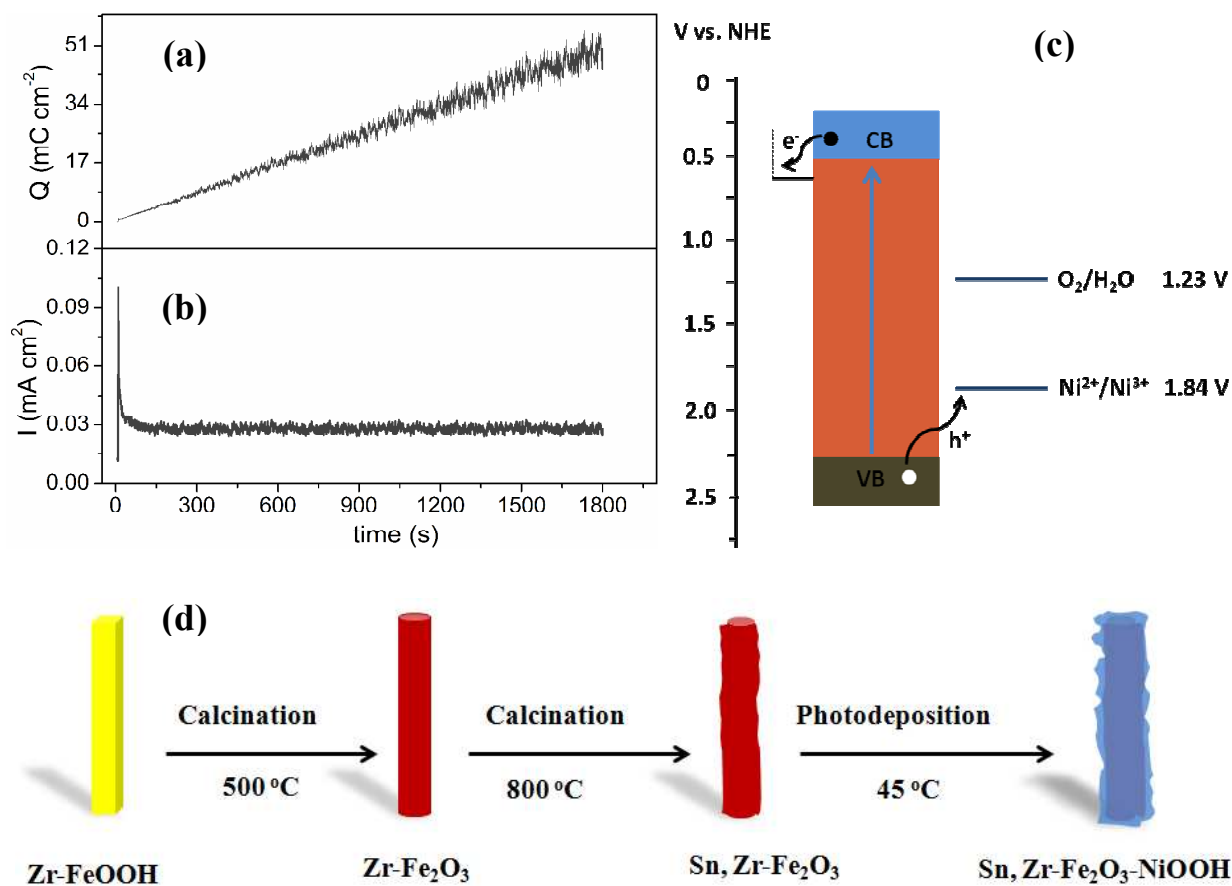


Figure 2. (a) The quantity of charge passed during photo-assisted electrodeposition of NiOOH. (b) Deposition curve of NiOOH on Fe₂O₃ electrode in 0.1 M NiSO₄ aqueous solution. (c) Schematic illustration of the oxidation potentials of N²⁺/Ni³⁺ and H₂O/O₂ relative to the band gap of Fe₂O₃. (d) Schematic illustration of the overall morphology evolution.

X-ray diffraction (XRD) measurements were carried out to examine the phase purity and crystallinity of each sample. In the XRD pattern of the β -FeOOH film (Figure 3(a)) three prominent peaks at 2θ value of 11.8, 35.0 and 56.0 ° are observed. These peaks are associated with the (110), (211) and (512) crystal planes of β -FeOOH (JCPDS card number 34-1266). After annealing at 500 °C, all the FeOOH diffraction peaks were vanished and new peaks at 2θ value of 35.7 and 64.0 ° have been emerged. These peaks are corresponding to (110) and (300) crystal planes of α -Fe₂O₃ (JCPDS card number 33-0664), revealing the complete conversion of β -FeOOH to α -Fe₂O₃. Strong (110) diffraction peak implies that the hematite nanorods are highly oriented in the [110] direction on the substrate. The (110) peak intensity of both monodoped (Sn) Fe₂O₃ and codoped (Sn, Zr) Fe₂O₃ calcined at 800 °C is much higher than that of their corresponding samples annealed at 500 °C (i. e. without unintentional Sn doping), indicating enhanced crystallinity of samples calcined at 800 °C. In addition, we further estimated the average crystallite size present in Fe₂O₃ nanorods from the full width at half maximum (FWHM) value of the more intense (110) XRD peak using Scherrer's equation.²⁶

$$D = \frac{0.94\lambda}{\beta \cos\theta} \quad (1)$$

where β is the FWHM, θ is the Bragg angle and λ is the wavelength of X-ray. The full-width at half-maximum (FWHM) values of the (110) peak of Fe₂O₃ calcined at 500 and 800 °C were found to be 0.004939 and 0.003875 rad., respectively. By applying the above mentioned equation, average crystallite size increased from 30.82 to 39.28 nm when annealing temperature increased from 500 to 800 °C. Moreover no peak shift, broadening and additional peaks appeared in the XRD patterns of both monodoped and codoped samples after 800 °C annealing. For XRD analysis of the NiOOH decorated codoped (Sn, Zr) Fe₂O₃ sample the NiOOH film was deposited continuously for 5 hours to increase its loading content and the result is presented in Figure 3(b). The XRD peak at 11.6 ° is indexed to the (003) crystal plane of γ -NiOOH according to JCPDS card no. 06-0075.²⁷ The low intensity of this peak results from the low crystalline nature of the NiOOH film. The optical properties of samples were measured with UV-Vis diffuse reflectance

spectroscopy (DRS). Figure 3(c) illustrates the UV–vis absorbance spectra of Fe_2O_3 samples annealed at 500 and 800 °C (i. e. without and with Sn doping respectively). It is shown that the absorption edge of Fe_2O_3 film annealed at 800 °C showed significant red shift compared to 500 °C annealed film which is attributed to unintentional Sn doping. The corresponding band gap of the samples were determined and the results were found to be 2.11 and 2.06 eV for undoped and Sn doped Fe_2O_3 samples respectively (Figure S3(a)), Further experimental details are given in the supplementary material). On the other hand, Figure 3(d) shows that the absorption spectra of both monodoped (Sn) Fe_2O_3 and codoped (Sn, Zr) Fe_2O_3 were identical, indicating no change in band gap of Fe_2O_3 upon intentional doping of Zr. Moreover, no significant change in absorption intensity and absorption edge was observed after NiOOH has been deposited.

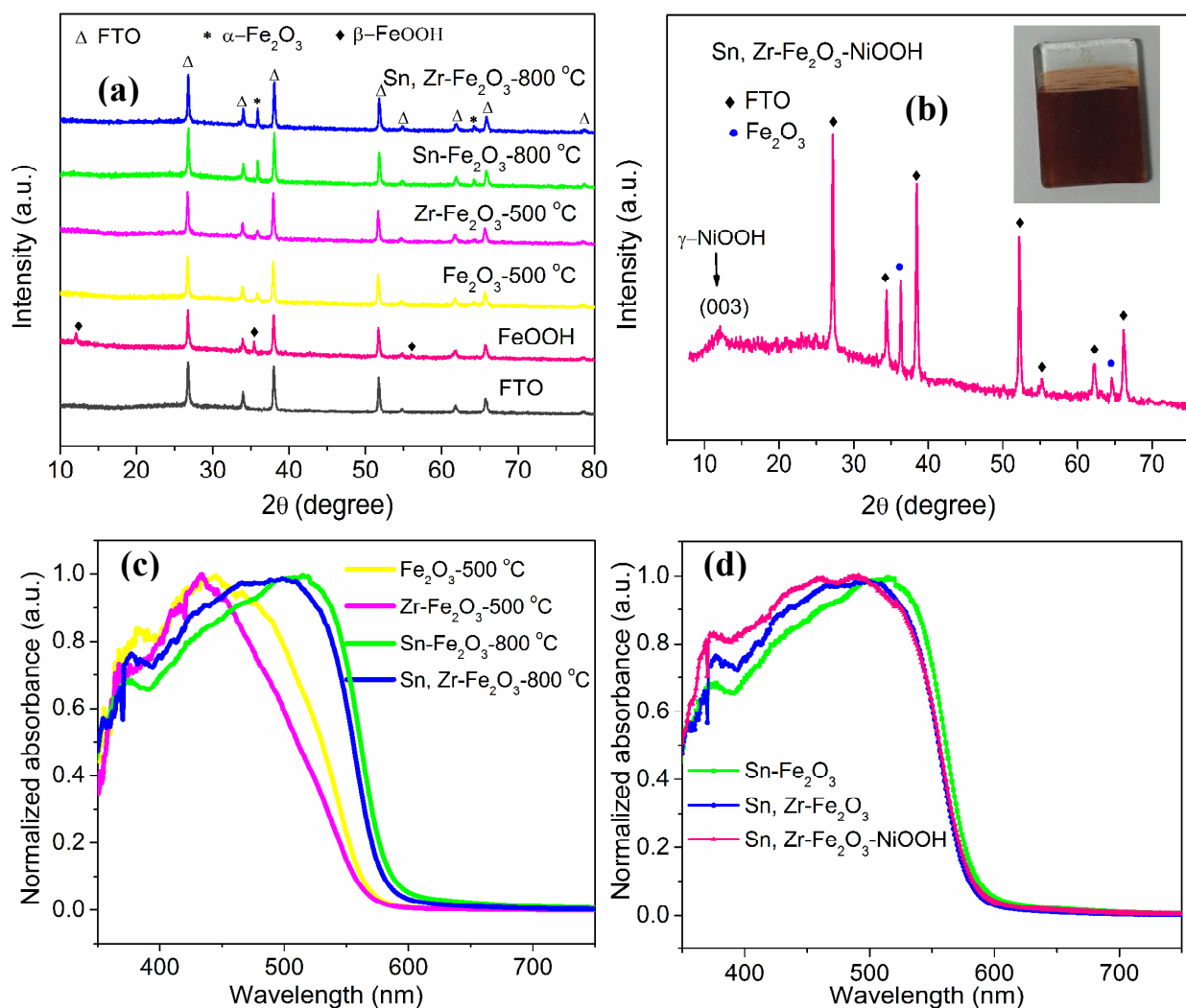
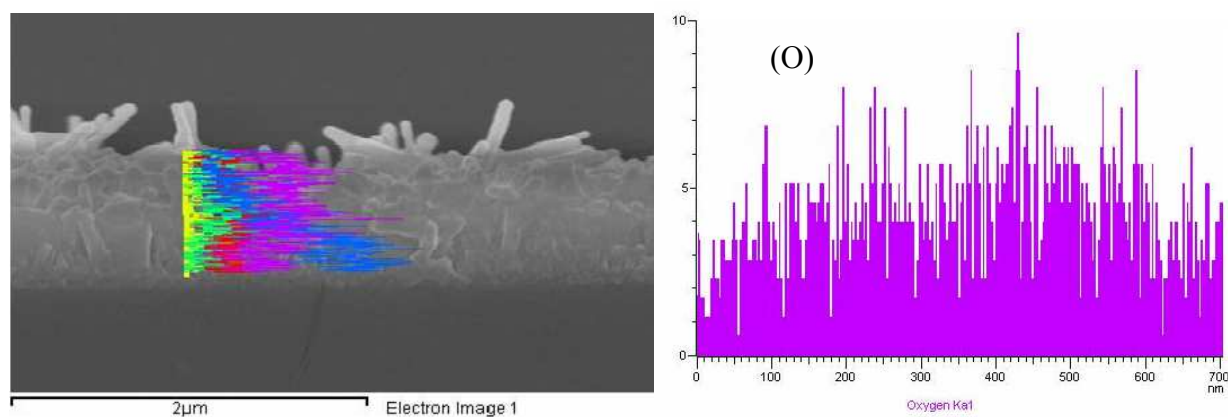


Figure 3. (a) XRD patterns collected for FTO, FeOOH and Fe₂O₃ samples. (b) XRD pattern of codoped (Sn, Zr) Fe₂O₃ after 5 h deposition of NiOOH. Inset: digital picture of NiOOH coated codoped (Sn, Zr) electrode. (c) and (d) Normalized UV–visible absorption spectra.

The approximate cross-sectional atomic distribution of NiOOH modified codoped (Sn, Zr) Fe₂O₃ was determined from EDX line scanning (Figure 4) using axial scanning from the top to the bottom of the film cross-section. The results confirm that both Fe and O have nearly uniform atomic distribution along the cross-section of the electrode. The EDX line scan of Sn revealed that its amount gradually increases from the top surface to the bottom of the electrode. This is strong evidence that shows the diffusion of Sn from the FTO conductive substrate to the Fe₂O₃ film during high temperature annealing. It has been found that high concentration of Sn is found at the near-substrate region of the Fe₂O₃ electrode and its concentration gradually decreases towards the surface of the electrode. This gradual distribution of tin creates a typical gradient doping into Fe₂O₃ bulk and helps to improve the carrier separation. On the other hand zirconium, which is primarily added to the precursor solution, showed uniform atomic distribution along the film thickness. This helps to introduce additional majority carriers into the entire film and improve the electrical conductivity of the electrode. Uniform distribution of Ni along the film cross-section was seen in the Ni line scan. This indicates the benefit of using photodeposition over that of electrodeposition to deposit NiOOH co-catalyst uniformly on Fe₂O₃.



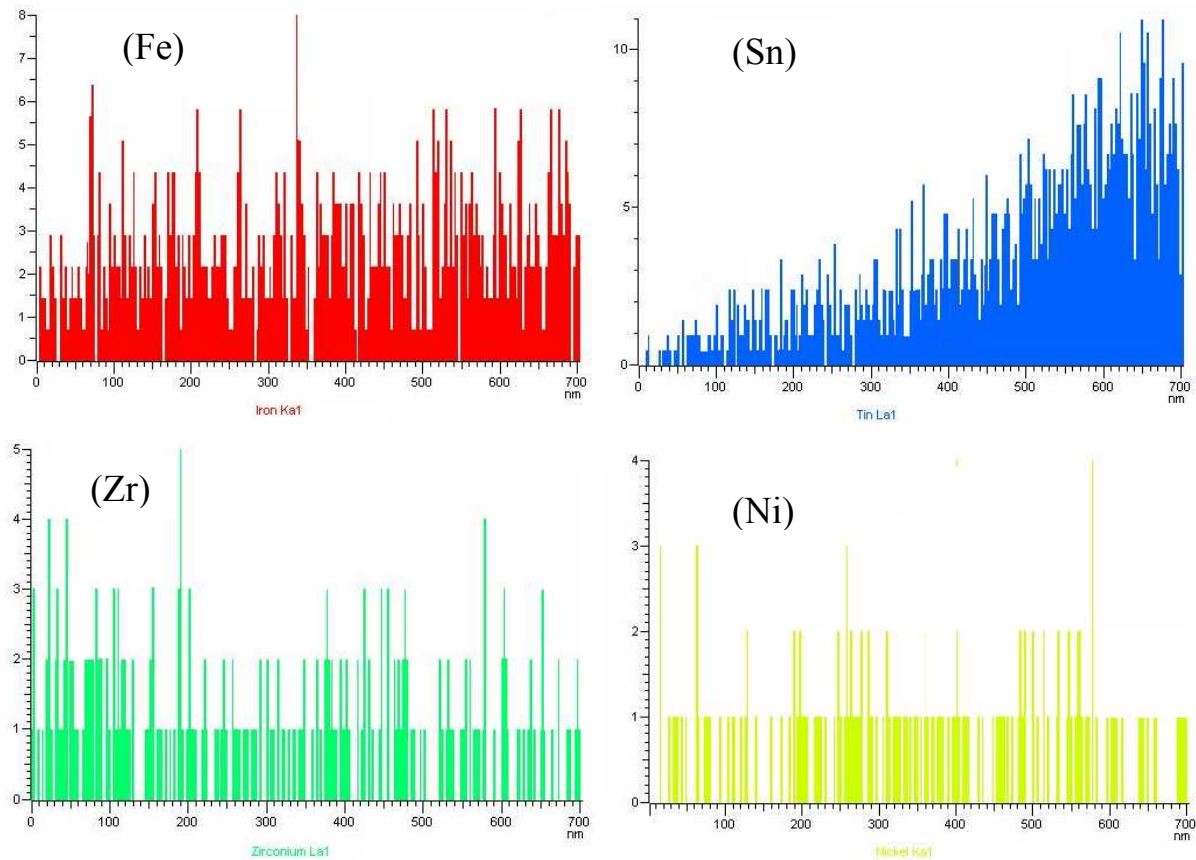


Figure 4. Cross-sectional SEM image of NiOOH modified codoped (Sn, Zr) Fe_2O_3 associated with EDS line scan and cross-sectional atomic distribution of oxygen, iron, tin, zirconium and nickel atoms.

In this study, all photoelectrochemical experiments were performed using standard three electrode configuration in 1 M NaOH electrolyte solution. Figure 5(a) shows photocurrent density-potential (J- V) curves of monodoped (Sn) Fe_2O_3 , codoped (Sn, Zr) Fe_2O_3 and NiOOH modified codoped (Sn, Zr) Fe_2O_3 under dark and illumination using AM 1.5G simulated solar light. Each curve has been examined based on two prominent features, the photocurrent onset potential and saturated photocurrent density observed at the thermodynamic potential of the water oxidation reaction (1.23 V). First, we examined the PEC performance of pristine Fe_2O_3 electrodes annealed at 500 °C which showed negligible photocurrent density ($<0.03 \text{ mA cm}^{-2}$) at 1.23 V (Figure S4(c)). Whereas Fe_2O_3 annealed at 800 °C showed dramatically higher photocurrent (0.86 mA cm^{-2}) at 1.23 V (Figure 5(a)). This remarkable enhancement stem from enhanced crystallinity (evidenced from XRD pattern) and unintentional Sn doping which

diffuses from the FTO layer to Fe_2O_3 bulk. The later has been reported previously by a number of studies. For example, Sivula et al reported that the enhanced photocurrent density obtained from hematite photoanode is partly caused by Sn doping that originates from the FTO substrate during high temperature treatment.¹⁸ Electronic structure calculations showed that doping of Fe_2O_3 with Sn leads to improved PEC activities that arises from enhanced electrical conductivity due to the reduction of electron effective mass at the conduction band minimum.²⁸ However, in this study we have found that the diffusion of Sn causes high to low (from bulk to surface) gradient re-distribution. This might create a vertical potential distribution along the length of nanorods which facilitates easy transfer of photogenerated electrons to the current collector and thereby enhance the charge separation efficiency. Although high-temperature sintering can introduce Sn from the FTO substrate into hematite to form gradient doping, the loss of Sn will significantly diminish the electrical conductivity of the FTO substrate. Applying a short annealing time (20 min) overcomes this tradeoff by limiting the amount of Sn diffused without significant glass deformation. Recently, Ling et al. studied the effect of Sn doping on the morphology and electronic properties of hematite nanostructures by synthesizing intentionally and unintentionally Sn-doped hematite nanocorals and nanowires respectively.¹ They have found that intentionally Sn doped hematite nanocorals showed 1.5 times higher photocurrent density than unintentionally Sn-doped hematite nanowires, which was ascribed to the improved electrical conductivity and increased surface area of nanocorals. However, the intentional Sn doping is also accompanied with unintentional Sn diffusion. More over the dopant precursor solution completely changed the nanowire morphology to nanocorals.

Figure 5(a) also shows that the codoped (Sn, Zr) Fe_2O_3 samples demonstrated significantly much higher photocurrent density (1.34 mA cm^{-2}) at 1.23 V when compared to the monodoped (Sn) Fe_2O_3 photoanode. Zr dopant introduces additional photoelectrons and improves the electrical conductivity of the electrode. Each Zr atom donates one electron to Fe (in hematite), forming Fe^{2+} and Zr^{4+} , thereby increasing the carrier concentration. Compared to the widely used Ti dopant, Zr does not trap carriers due to less stable Zr^{3+} than Ti^{3+} . According to ab initio quantum mechanics calculations done by Liao and coworkers, the use of n-type zirconium dopant do not act as electron trapping sites due to the higher instability of Zr^{3+} and therefore can provide more charge carriers without inhibiting transport.²² Shen et al also reported Zr doped Fe_2O_3 nanorod arrays for PEC water splitting.²¹ However the codoping effect of unintentional diffused Sn,

which plays a significant role on the improved PEC performance, has not been considered in their study. We have determined the optimum amount of Zr by varying the amount of ZrCl_4 added to the precursor solution (Figure S4). The results revealed that the photocurrent density increased to 0.99 mA cm^{-2} for 0.5% atomic dopant concentration of Zr. Highest photocurrent density (1.34 mA cm^{-2}) was achieved at 1.5% atomic dopant concentration which is 1.56 times higher than that of the monodoped (Sn) Fe_2O_3 photoanode. Increasing the amount of Zr dopant to 2% and 3% caused decrease in the photocurrent density to 1.17 and 0.83 mA cm^{-2} respectively. The results confirm that the enhanced photocatalytic activity of codoped (Sn, Zr) Fe_2O_3 nanorods is limited to lower atomic dopant concentration of Zr. However, previous theoretical study showed that the measured solubility of Zr in Fe_2O_3 can extend up to 10 atomic percent without forming a new phase.²⁰ This contradiction might arise from the n-type Zr and Sn dopants that can introduce more number of majority carriers to Fe_2O_3 at high doping concentration. This leads to reasonable electron-hole recombination, resulting lower PEC performance.

To enhance the poor oxidation kinetics of hematite we employed NiOOH as a surface modification. Recently NiOOH has been synthesized and implemented for various energy harvesting applications. For example, Kim and Choi investigated the effect of dual OER catalyst layers, FeOOH and NiOOH, on the interfacial recombination, water oxidation kinetics, and the Helmholtz layer potential drop at the OER catalyst/electrolyte junction.⁹ Zhang et al also prepared 3D nanoporous NiOOH thin film on to TiO_2 nanoarray substrates by photodeposition technique for energy storage and conversion applications.²⁹ When the codoped (Sn, Zr) Fe_2O_3 photoanode was modified with NiOOH co-catalyst (deposited using photo-assisted electrodeposition), its photocurrent density was increased by 23% (to 1.65 mA cm^{-2}) at 1.23 V (Figure 5(a)). More importantly, high photocurrent density was achieved in the kinetic control region. The sharp rise beyond the onset potential and the tendency of saturation in the high potential region indicate high charge transfer and collection efficiency in the NiOOH modified codoped (Sn, Zr) Fe_2O_3 photoanode. In the potential range of 0.8 to 1 V, the NiOOH modified codoped (Sn, Zr) Fe_2O_3 photoanode achieved photocurrent density that varied from 0.4 to 1.0 mA cm^{-2} , which is 150 to 400% higher compared to that of the codoped (Sn Zr) Fe_2O_3 sample. The PEC performance of codoped (Sn, Zr) Fe_2O_3 modified with electrodeposited NiOOH was also examined (Figure S4(b)). The saturated photocurrent density lowered to 1.3 mA cm^{-2} at 1.23 V compared to the one modified with photo-assisted electrodeposited NiOOH. The dense

NiOOH layer formed on the surface of Fe_2O_3 (Figure 1(f)) limits the access of electrolyte to the bottom layer of the electrode which reduces the amount of charge reaching the electrode/electrolyte interface.

Another imperative feature of J-V curve is the onset potential. The Codoped (Sn, Zr) Fe_2O_3 sample showed a slight anodic shift of photocurrent onset potential from 0.70 to 0.74 V, compared to monodoped (Sn) Fe_2O_3 nanorods samples. This phenomenon has been clearly seen in charge injection efficiency results, whereby the codoped (Sn, Zr) Fe_2O_3 photoanode showed lower charge injection efficiency than monodoped (Sn) Fe_2O_3 nanorods at lower potential. Consequently we found it very important to combine the codoped (Sn, Zr) Fe_2O_3 photoanode with an efficient oxygen evolving catalyst. As evidenced from J-V results (inset of Figure 5(a)) the codoped Fe_2O_3 photoanode showed a cathodic shift of 160 mV in onset potential (i. e. from 0.74 to 0.58 V) after NiOOH has been deposited. This is the lowest onset potential reported for surface modified Fe_2O_3 photocatalyst in 1M NaOH. Under the same reaction conditions, this value is 40 mV lower than the most efficient nickel based co-catalyst, NiFeO_x , recently demonstrated on hematite for photoelectrochemical water splitting purposes.³⁰ To show where the performance of our photoanode stands, we plot a road map which summarizes the progress of onset potential improvements of some recent Fe_2O_3 based photoanodes presented in terms of current density generated under standard condition (1 sun illumination) (Figure S6, the following references are included in parentheses³¹⁻⁴⁰). It summarizes few reports which target on surface treatment of Fe_2O_3 photoanodes with co-catalysts, over layers, and other chemical modification strategies. The onset potential ranges from 0.6 to 1.0 V vs. RHE, indicating that the NiOOH we employed is an efficient co-catalyst for water oxidation. The dark current water oxidation onset potential of all photoanodes was also measured and the results are shown in Figure 5(a). Nearly the same dark current onset was obtained for monodoped (Sn) and codoped (Sn, Zr) Fe_2O_3 photoanodes at 1.63 V, indicating similar electrocatalytic activity for water oxidation. However, the dark current onset potential of the NiOOH modified codoped (Sn, Zr) Fe_2O_3 photoanode showed a cathodic shift to 1.46 V, which shows a similar trend to that of the cathodic shift of onset potential observed under illumination. The results suggest that the cathodic shift of onset potential in the NiOOH modified codoped (Sn, Zr) Fe_2O_3 photoanode generally come from accelerating water oxidation kinetics.

To verify that the measured photocurrent of the NiOOH modified codoped Fe₂O₃ photoanode originates from water splitting or from any undesired side reactions, we carried out gas evolution measurements under AM 1.5G (100 mW cm⁻²) simulated solar light illumination. The amount of O₂ gas evolved was collected and measured every 30 minute time interval. For a 3 h continuous photocatalytic reaction time, we observed a Faradaic efficiency of 90 to 96%. Thus, more than 90% of the photogenerated charges were consumed for water splitting and hydrogen/oxygen production. (The details are given in the supplementary material). It should also be noted that, for a photocatalyst to be commercially viable, stability and high activity of the photocatalyst are both indispensable. It is well known that Fe₂O₃ is stable in neutral and alkaline electrolytes under PEC operating conditions. The stability of NiOOH modified codoped (Sn, Zr) Fe₂O₃ photoanode also demonstrated excellent stability for a continuous 10 h irradiation without the addition of sacrificial reagent (Figure 5(d)). After 10 h continuous PEC operation, 94.1% of the initial photocurrent was maintained, indicating its excellent stability.

Achieving considerable photocurrent density at low applied potential and/or high saturation photocurrent density is another key issue to increase the overall PEC hydrogen generation efficiency of photocatalysts. Hence, the PEC water splitting efficiency of the samples was quantitatively evaluated using applied bias photon-to-current efficiency (ABPE) based on the equation:

$$\text{ABPE (\%)} = \left[\frac{|j_{\text{ph}}| (\text{mA/cm}^2) (1.23 - |V_b|) (\text{V})}{P_{\text{total}} (\text{mW/cm}^2)} \right]_{\text{AM 1.5G}} \times 100 \quad (2)$$

where V_b is the applied bias vs. RHE, J_{ph} is the photocurrent density at the measured potential, and P_{total} is the power density of incident light. A maximum photoconversion efficiency of 0.243% was achieved for NiOOH modified codoped (Sn, Zr) Fe₂O₃ photoanode at 0.94 V vs. RHE, which was 2.5 and 1.69 times higher than that of the monodoped (Sn) Fe₂O₃ and codoped (Sn, Zr) Fe₂O₃ samples respectively (Figure 5(c)). Another interesting feature of this is that, the maximum photoconversion efficiency was obtained at lower applied potential compared with the monodoped and codoped samples. This is associated with reduction of hole injection barrier at Fe₂O₃/electrolyte interface by NiOOH layer.

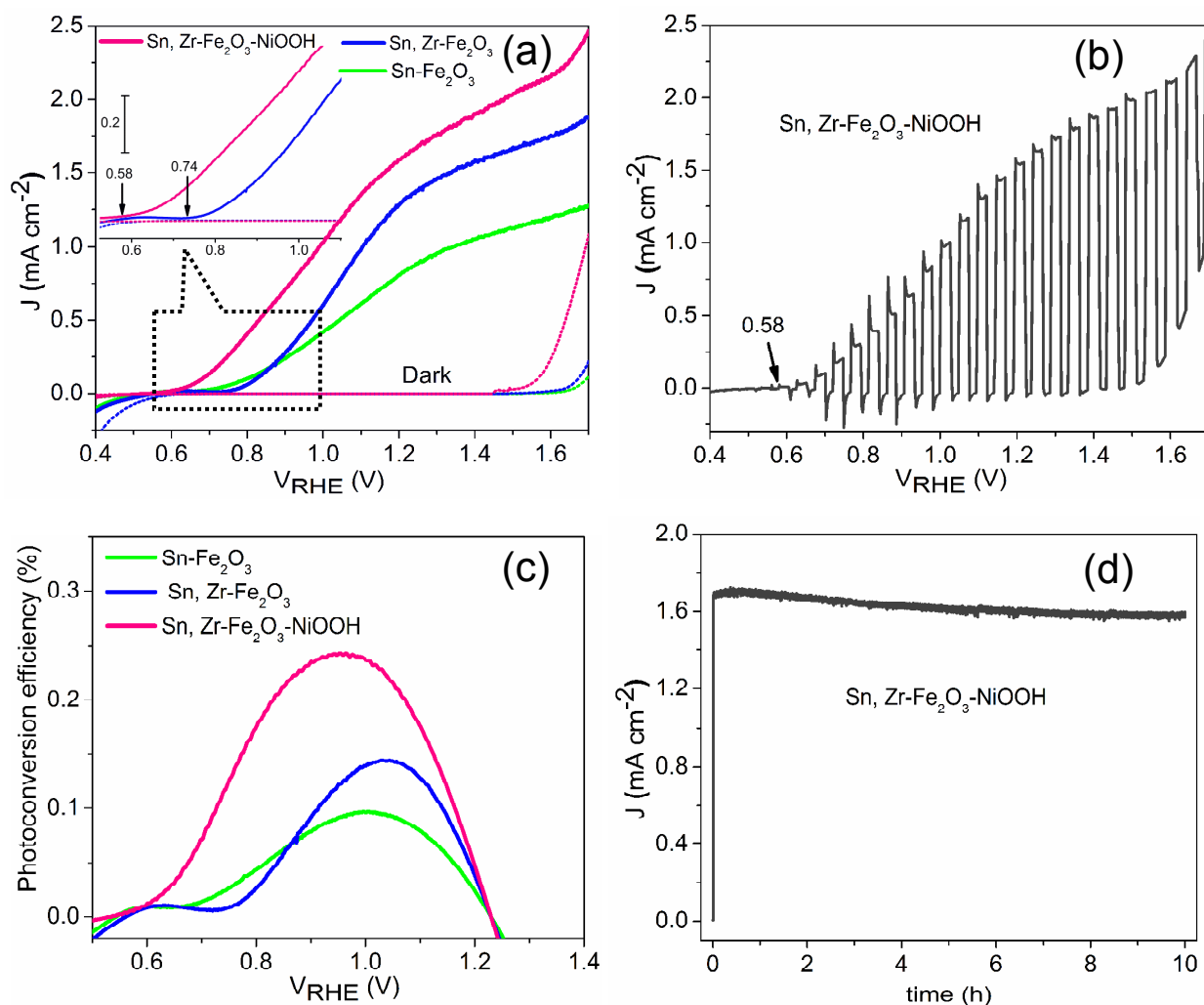


Figure 5. (a) Photocurrent density as a function of applied potential in dark and illumination. (b) photo/dark current density as a function of applied potential in on/off interrupted illumination. (c) photoconversion efficiencies as a function of applied potential. (d) photocurrent density–time plot measured at 1.23 V. All measurements were performed under 1 sun simulated light illumination (AM 1.5G, 100 mW cm⁻²).

To understand the interplay between the PEC activity and the light absorption properties of samples, we examined their PEC activity as a function of wavelength. The IPCE spectrum of each electrode was measured in 1 M NaOH as a function of incident photon wavelength at 1.23 V under monochromatic illumination calibrated by standard silicon photodiode (Newport model 818-UV). The IPCE was calculated using the following equation.

$$\text{IPCE (\%)} = \frac{J_{\text{ph}} (\text{mA/cm}^2) \times 1240 (\text{ev} \times \text{nm})}{P_{\text{mono}} (\text{mW/cm}^2) \times \lambda (\text{nm})} \times 100 \quad (3)$$

Where J_{ph} is the photocurrent density, P_{mono} is the intensity of the incident monochromatic light, and λ is the wavelength of the monochromatic light. To prevent overestimation of the efficiency due to increased active area of the electrode, we use an optical fiber with a 1 cm² aperture. Therefore all the photons from an optical fiber go into a sample cell. The IPCE spectra of the samples are shown in Figure 6(a). Compared to the monodoped (Sn) Fe₂O₃ sample, the codoped (Sn, Zr) Fe₂O₃ photoanode exhibited enhanced IPCE. Further enhancement in IPCE was achieved after codoped (Sn, Zr) Fe₂O₃ photoanode has been modified with NiOOH. The photocurrent response spectrum of NiOOH modified codoped (Sn, Zr) Fe₂O₃ photoanode exhibits higher but similar features with that of both the codoped (Sn, Zr) Fe₂O₃ and monodoped (Sn) Fe₂O₃ photoanodes, indicating the primary photo-response is from the Fe₂O₃ nanostructure and not the NiOOH itself. The enhancement is associated with the improved charge transport characteristics (It will be discussed later) and the role of NiOOH in facilitating effective use of photogenerated holes for water oxidation at the electrode/electrolyte interface.

To further shed light on understanding the charge transfer dynamics of the photoanodes, we determine charge transport and charge injection efficiencies using 0.5 M H₂O₂ hole scavenger added to 1 M NaOH electrolyte solution.^{7, 8} The key assumption for this approach is that the oxidation kinetics of H₂O₂ is very fast and its charge transfer (injection) efficiency is 100% or the surface recombination of charges is assumed to be eliminated. The water splitting photocurrent ($J_{\text{ph}}^{\text{H}_2\text{O}}$) is a product of the rate of photon absorption expressed as a current density (J_{abs}), the charge separation yield of the photogenerated carriers (η_{sep}), and charge injection efficiency to the electrolyte (η_{inj}):

$$J_{\text{ph}}^{\text{H}_2\text{O}} = J_{\text{abs}} \times \eta_{\text{sep}} \times \eta_{\text{inj}} \quad (4)$$

In the presence of H₂O₂, $\eta_{\text{inj}}=1$, because surface recombination is assumed to be completely suppressed. Hence, the photocurrent density in the presence of H₂O₂ ($J_{\text{ph}}^{\text{H}_2\text{O}_2}$) is given by:

$$J_{\text{ph}}^{\text{H}_2\text{O}_2} = J_{\text{abs}} \times \eta_{\text{sep}} \quad (5)$$

Therefore,
$$\eta_{sep} = J_{ph}^{H_2O_2} / J_{abs} \quad (6)$$

Combining equation 3 and 4 results in:

$$\eta_{inj} = J_{ph}^{H_2O} / J_{ph}^{H_2O_2} \quad (7)$$

J_{abs} (photocurrent assuming 100% APCE) is determined by integrating the UV–vis absorption spectra (Figure 3(d)) of the samples with respect to the AM 1.5G solar light spectrum.⁷ Using this calculation the J_{abs} values for monodoped (Sn) Fe_2O_3 , codoped (Sn, Zr) Fe_2O_3 , and NiOOH modified codoped (Sn, Zr) Fe_2O_3 photoanodes were found to be 8.5, 8.04 and 8.76 respectively. The photocurrent responses of all the samples with and without H_2O_2 are provided in the supplementary material (Figure S6). Without H_2O_2 and at low applied bias, surface recombination, which originates from surface states and interface barriers, is the dominant effect in water oxidation reaction. Thus the photocurrent response becomes lower. Once H_2O_2 is added to the electrolyte, such surface barriers become less effective, rather bulk recombination becomes the limiting factor and the photocurrent approaches a plateau. In all the photoanodes, the saturated photocurrents in NaOH and NaOH + H_2O_2 electrolyte systems were nearly the same, since the addition of H_2O_2 does not significantly affect the light absorption, pH or flat band potentials of the photoanodes. This indicates that no current doubling occurs in the presence of H_2O_2 , and it justifies the presumption of constant J_{abs} and η_{sep} for $J_{ph}^{H_2O_2}$ and $J_{ph}^{H_2O}$.

Figure 6(b) and (c) illustrate the charge separation (η_{sep}) and injection efficiencies (η_{inj}) respectively. As shown in Figure 6(b), the charge separation efficiency of monodoped (Sn) Fe_2O_3 , codoped (Sn, Zr) Fe_2O_3 and NiOOH modified codoped (Sn, Zr) Fe_2O_3 photoanodes was found to be 12.5, 19.9 and 24.8% at 1.23 V vs. RHE respectively. Compared to monodoped (Sn) Fe_2O_3 , the 1.6 times higher η_{sep} of codoped (Sn, Zr) Fe_2O_3 photoanodes is associated with the improved electrical conductivity due to addition of extra photoelectrons from Zr. Compared to other metal oxide photoanodes such as TiO_2 , WO_3 and $BiVO_4$, Fe_2O_3 exhibited lower charge separation efficiency due to its very short excited state life time characteristics. Figure 6(c) shows charge injection efficiency as a function of the applied potential. NiOOH modified codoped (Sn, Zr) Fe_2O_3 photoanode exhibited significantly higher charge injection efficiency at lower potential range which is correlated with the cathodic shift of onset potential observed in J-V curves (Figure 5(a)). For example, at 0.8 V NiOOH modified codoped (Sn, Zr) Fe_2O_3

photoanode showed η_{inj} of 40.7%. This value is 2.6 and 6.2 times higher than that of monodoped (Sn) Fe_2O_3 (η_{inj} , 6.6%) and codoped (Sn, Zr) Fe_2O_3 (η_{inj} , 15.7%) photoanodes respectively. This is remarkable achievement to split water at low applied bias. It is also strong evidence that charge injection barrier can be greatly suppressed by NiOOH coating. The charge injection efficiency results are also supported by the chopped light transient photocurrent measurements (Figure 7) at different potential.

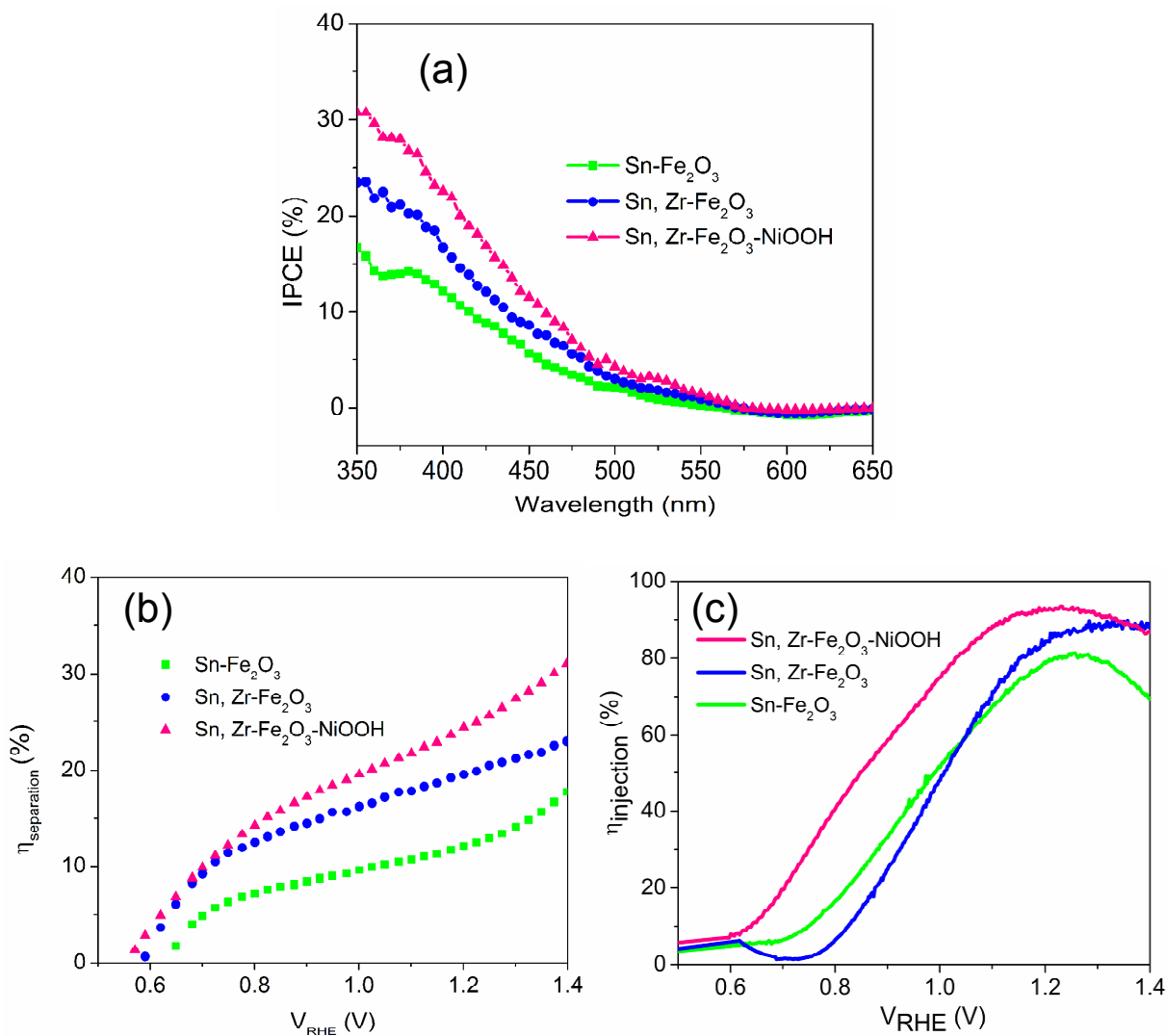


Figure 6. (a) IPCE spectra obtained at 1.23 V vs. RHE applied potentials. (b) Charge separation efficiency (η_{sep}) as a function of applied potential. (c) Charge injection efficiency (η_{inj}) as a function of applied potential.

Mott-Schottky analysis is employed to determine the donor density and flat band potential of the electrodes (assuming flat photoelectrodes) by measuring the capacitance of the space charge region formed at the semiconductor/electrolyte interface at a fixed frequency of 10^3 Hz using the following equation.

$$\frac{1}{C^2} = \frac{2}{\epsilon\epsilon_0 A^2 e N_D} \left(V - V_{fb} - \frac{k_B T}{e} \right) \quad (8)$$

Here C is the space-charge capacitance of the semiconductor, ϵ is the dielectric constant of hematite (80),⁴¹ ϵ_0 is the permittivity of vacuum (8.854×10^{-12} C V⁻¹ m⁻¹), A is the area of the electrode, e is the electronic charge (1.602×10^{-19}),⁴² N_D is the number of donors density, V is the applied voltage, V_{fb} is the flat band potential, k_B is Boltzmann's constant, and T is the absolute temperature. Some assumption are made in the derivation of the Mott-Schottky equation, thus a standard nonlinear relationship between $1/C^2$ and V may not be observed if such assumptions are not fulfilled (i.e. the space-charge region capacitance much less than the Helmholtz layer capacitance, flat surface, absence of surface states, frequency-independence of the dielectric constant ϵ , homogeneous spatial distribution of donors/acceptors).^{43, 44} The flat band potentials were determined from the intercepts of $1/C^2$ vs. V by subtracting $k_B T/e = 0.025$ V from the intercept. The charge carrier (donor) density (N_D) is calculated from the slope of the $1/C^2$ vs. V curve using the following equation.

$$N_D = \left(\frac{2}{\epsilon\epsilon_0 e} \right) [d(1/C^2)/d(V)]^{-1} \quad (9)$$

All the samples exhibited positive slopes (Figure 7(a)), indicating n-type semiconductors. The measured flat-band potentials (V_{fb}) were used to obtain the absolute band-edge positions with respect to the water redox potentials. As depicted from table 1, the V_{fb} values of monodoped (Sn) Fe_2O_3 , codoped (Sn, Zr) Fe_2O_3 and NiOOH modified codoped (Sn, Zr) Fe_2O_3 electrodes did not show significant difference between each other. However the photocurrent onset potential of codoped (Sn, Zr) Fe_2O_3 photoanode showed slight anodic shift compared to the monodoped sample in the J-V curve. This trade-off arises from the difference in surface catalytic properties of the photoelectrodes. Similarly, the photocurrent onset potential of NiOOH modified codoped (Sn, Zr) Fe_2O_3 electrode showed 160 mV cathodic shift while its V_{fb} was kept nearly the same as that of both the monodoped and codoped photoanodes. This is additional evidence that NiOOH

accelerates the water oxidation kinetics of Fe_2O_3 without altering the band edge positions. Due to the enhanced transfer of photogenerated holes to the NiOOH layer, recombination of holes with conduction band electrons would be significantly reduced. Hence, the photocurrent onset potential shows significant cathodic shift. We also noted that the V_{fb} obtained from the Mott–Schottky plot is somewhat more negative than the photocurrent onset potential in the J-V curves. This is associated with the recombination of accumulated photogenerated holes and electrons at the electrode surface at lower potential region, since lower applied potential is not enough to drive all the photogenerated holes to the electrolyte solution. The carrier concentration (N_D) of monodoped (Sn) Fe_2O_3 photoanode is in a good agreement with other literature reports.¹ On the other hand, the codoped (Sn, Zr) Fe_2O_3 photoanode achieved more than three times higher N_D than that of the monodoped (Sn) Fe_2O_3 photoanode. This is direct evidence that shows Zr doping as an electron donor that can apparently improve the electron transfer properties of the sample. However the N_D value of NiOOH modified codoped (Sn, Zr) Fe_2O_3 sample shows 1.4 times higher than that of codoped (Sn, Zr) Fe_2O_3 sample. This is associated with the formation of a highly capacitive NiOOH layer that can able to transfer photogenerated holes to the electrolyte. Consequently, recombination of the photogenerated holes with conduction band electrons will be significantly reduced and thereby the N_D value of the system becomes enhanced. In order to further examine the electrical conductivities of the samples, electrochemical impedance spectroscopy analyses were carried out. According to the Nyquist plots (Figure 7(b)), the electrodes exhibited semicircles with different radii. The capacitive arc of codoped (Sn, Zr) Fe_2O_3 photoanode has smaller radius than that of the monodoped (Sn) Fe_2O_3 photoanode, indicating smaller charge transfer resistance. Zr-doping promotes charge separation by introducing additional electrons and enhances the PEC water splitting performance. A much smaller radius was observed in NiOOH modified codoped (Sn, Zr) Fe_2O_3 photoanode, implying that NiOOH can greatly promote the charge transfer across the semiconductor/electrolyte interface resulting in suppressed surface electron-hole recombination.

Table 1: Electrical and photoelectrochemical properties of electrodes deduced from Mott-Schottky and J-V plots

Sample	N_D ($\times 10^{20} \text{ cm}^{-3}$)	V_{fb} (V) vs. RHE	Onset potential (V) vs. RHE
Sn-Fe ₂ O ₃	0.82	0.37	0.71
Sn, Zr-Fe ₂ O ₃	2.98	0.38	0.74
Sn, Zr-Fe ₂ O ₃ .NiOOH	4.19	0.40	0.58

Figure 7(c) shows a typical transient photocurrent measurement at different applied potentials. The photocurrent transients displayed positive and negative spikes under chopped illumination, which are characteristics of surface recombination. The positive photocurrent spikes are associated with accumulation of holes in the electrode space charge layer under illumination. Whereas, the negative photocurrent spikes are caused by recombination of accumulated holes with free electrons in the conduction band, resulting in a back flow of electrons from the external circuit to the photoanodes.⁷ The photocurrent transient curve of NiOOH modified codoped (Sn, Zr) Fe₂O₃ photoanode shows smaller positive and negative spikes compared to that of monodoped and codoped photoanodes, suggesting the suppression of electron-hole recombination. Both smaller photocurrent transient spikes and negative shift of onset potential highlight the importance of NiOOH for enhanced photo-induced charge transfer kinetics at the semiconductor/electrolyte interface. On the other hand, at the higher potential region the size of the photocurrent spikes diminished for all photoanodes, indicating better charge transfer to the electrolyte solution assisted by the higher applied potential. For comparison transient photocurrent measurement was carried out for NiOOH modified codoped (Sn, Zr) photoanode in the presence of 0.5 M H₂O₂ in the electrolyte solution. No photocurrent spike or photocurrent decay was observed; indicating 100% charge transfer (injection) efficiency (Figure 7(d)). It is also noticeable from Figure 7(e) that at a constant potential (1 V), the current decay (difference between initial current (I_i) and final current (I_f); $I_d=I_i-I_f$) decreases in the order of monodoped (Sn) Fe₂O₃, codoped (Sn, Zr) Fe₂O₃ and NiOOH modified codoped (Sn, Zr) Fe₂O₃ samples which is in a good agreement with the transient photocurrent measurements at variable potential.

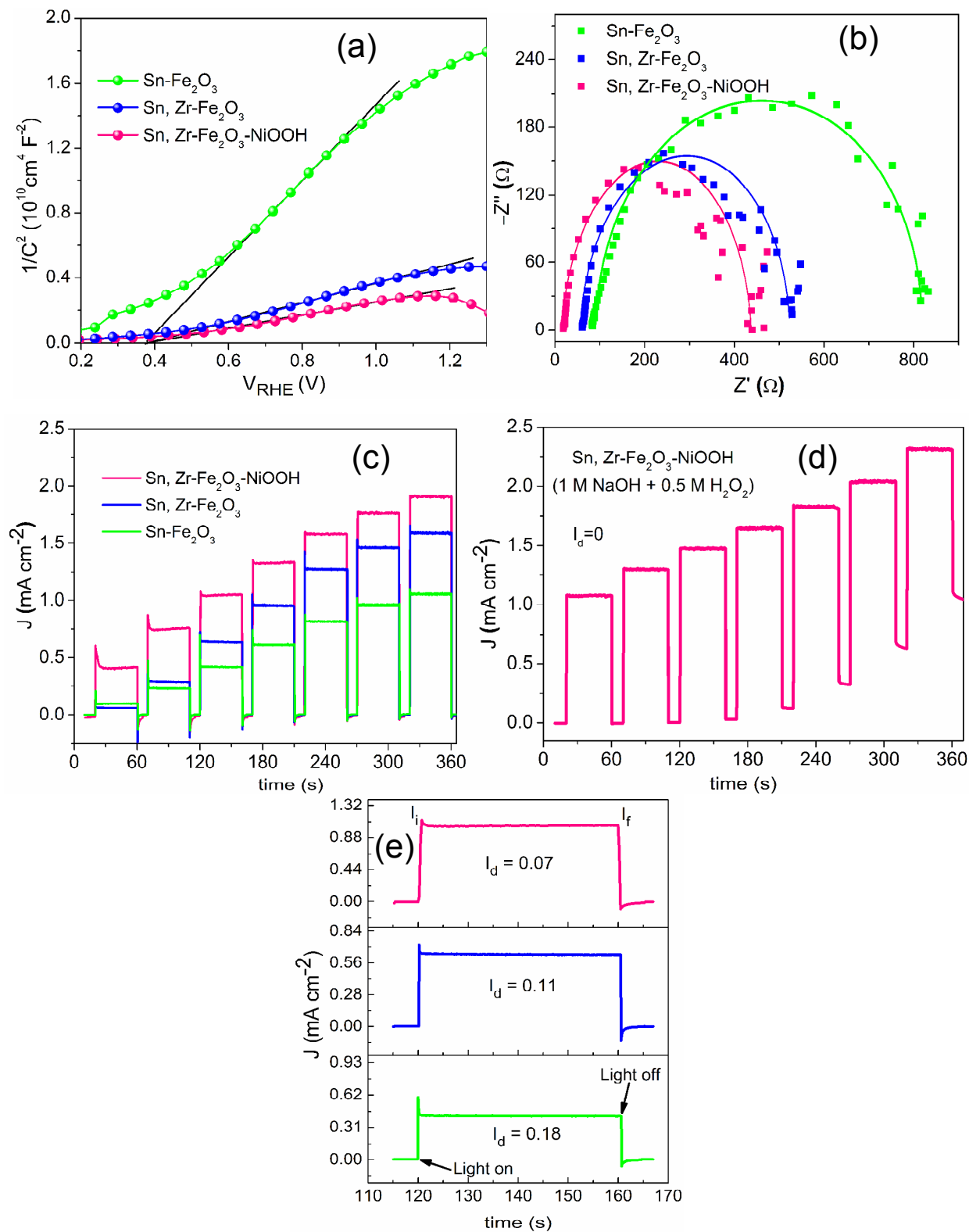


Figure 7. (a) Mott–Schottky plots measured in 1 M NaOH solution at 1 kHz Frequency. (b) Electrochemical impedance spectroscopy (EIS) Nyquist plots. (c) Transient photocurrent

measurement as a function of variable applied potentials (0.8, 0.9, 1, 1.1, 1.2, 1.3 and 1.4 V vs. RHE) in 1M NaOH electrolyte. (d) Transient photocurrent measurement as a function of variable applied potentials (0.8, 0.9, 1, 1.1, 1.2, 1.3 and 1.4 V vs. RHE) in 1 M NaOH + 0.5 M H₂O₂ electrolyte. (d) Transient photocurrent measurement as a function of constant applied potential (1 V vs. RHE) in 1M NaOH electrolyte.

Conclusion

In summary, a codoped (Sn, Zr) α -Fe₂O₃ photoanode modified with stable and earth abundant nickel oxyhydroxide (NiOOH) co-catalyst that can split water at low applied potential is reported. In this study, single-crystalline 1-D Fe₂O₃ nanorod arrays are synthesized by in-situ two step controlled annealing (at 500 and 800 °C) of 1-D β -FeOOH nanorod arrays grown directly on fluorine doped tin oxide (FTO) coated glass substrate via a simple solution-based method. We have found that high temperature annealing (800 °C) causes unintentional gradient Sn doping which greatly enhances the photoelectrochemical (PEC) activity of pristine Fe₂O₃. To enhance the conductivity of the sample further, Zr dopant was intentionally introduced. The codoped (Sn, Zr) Fe₂O₃ photoanode demonstrated 1.56 times higher photocurrent density (1.34 mA cm⁻²) at 1.23 V vs. RHE compared to monodoped (Sn) Fe₂O₃ photoanode. The remarkably improved electrical conductivity and more than three times higher charge carrier density (as evidenced from electrochemical impedance spectroscopy measurements and Mott-Schottky analysis) of the codoped (Sn, Zr) Fe₂O₃ photoanode highlighted the importance of codoping. Aiming to overcome the large overpotential of Fe₂O₃, NiOOH catalyst was deposited on to the codoped (Sn, Zr) Fe₂O₃ photoanode using facile photoassisted electrodeposition technique. The NiOOH modified codoped (Sn, Zr) Fe₂O₃ photoanode exhibited drastically lower onset potential (0.58 V) and a photocurrent density of 1.64 mA cm⁻² at 1.23 V. Interestingly a 160 mV cathodic shift in photocurrent onset potential was also observed. Its excellent stability was also demonstrated for a continuous 10 h PEC operation without addition of any sacrificial reagent. Concomitant with this, the NiOOH modified codoped (Sn, Zr) Fe₂O₃ photoanode exhibited 1.6 to 9.5 fold enhancement in charge injection efficiency (η_{inj}) at kinetic control region of 0.7 to 0.9 V compared to unmodified codoped photoanode. Finally, gas evolution measurements showed that the NiOOH modified codoped Fe₂O₃ photoanode achieved an average Faradaic efficiency of 93% indicating that most of the photogenerated charge carriers were consumed for water splitting.

Acknowledgements

The financial supports from the Ministry of Science and Technology (MoST) (103-2221-E-011-156-MY3, 103-3113-E-011 -001, 101-3113-E-011-002, 101-2923-E-011-001-MY3), the Ministry of Economic Affairs (MoEA) (101-EC-17-A-08-S1-183), and the Top University Projects of Ministry of Education (MoE) (100H451401), as well as the facilities supports from the National Synchrotron Radiation Research Center (NSRRC) and National Taiwan University of Science and Technology (NTUST) are acknowledged.

References

1. Y. Ling, G. Wang, D. A. Wheeler, J. Z. Zhang and Y. Li, *Nano Lett.*, 2011, 11, 2119-2125.
2. K. M. H. Young and T. W. Hamann, *Chem. Commun.*, 2014, 50, 8727-8730.
3. K. Sivula, F. Le Formal and M. Grätzel, *ChemSusChem*, 2011, 4, 432-449.
4. D. K. Bora, A. Braun and E. C. Constable, *Energy & Environ. Sci.*, 2013, 6, 407-425.
5. L. Wang, C.-Y. Lee, R. Kirchgeorg, H. Hildebrand, J. Muller, E. Spiecker and P. Schmuki, *Mater. Horiz.*, 2014, 1, 344-347.
6. Y. Qiu, S.-F. Leung, Q. Zhang, B. Hua, Q. Lin, Z. Wei, K.-H. Tsui, Y. Zhang, S. Yang and Z. Fan, *Nano Letters*, 2014, 14, 2123-2129.
7. H. Dotan, K. Sivula, M. Gratzel, A. Rothschild and S. C. Warren, *Energy & Environ. Sci.*, 2011, 4, 958-964.
8. F. F. Abdi, L. Han, A. H. M. Smets, M. Zeman, B. Dam and R. van de Krol, *Nat Commun*, 2013, 4, 1-5.
9. T. W. Kim and K.-S. Choi, *Science*, 2014, 343, 990-994.
10. F. E. Osterloh, *Chem. Soc. Rev.*, 2013, 42, 2294-2320.
11. Y. Hou, F. Zuo, A. Dagg and P. Feng, *Nano Lett.*, 2012, 12, 6464-6473.
12. E. Thimsen, F. Le Formal, M. Grätzel and S. C. Warren, *Nano Lett.*, 2010, 11, 35-43.
13. K. Kim, M.-J. Kim, S.-I. Kim and J.-H. Jang, *Sci. Rep.*, 2013, 3.
14. M. J. Katz, S. C. Riha, N. C. Jeong, A. B. F. Martinson, O. K. Farha and J. T. Hupp, *Coord. Chem. Rev.*, 2012, 256, 2521-2529.

15. A. K. Agegnehu, C.-J. Pan, J. Rick, J.-F. Lee, W.-N. Su and B.-J. Hwang, *J. Mater. Chem.*, 2012, 22, 13849-13854.
16. A. A. Dubale, W.-n. Su, A. G. Tamirat, C.-J. Pan, B. A. Aragaw, H.-M. Chen, C.-H. Chen and B. J. Hwang, *J. Mater. Chem. A*, 2014, DOI: 10.1039/C4TA03464C.
17. Y. Lin, S. Zhou, S. W. Sheehan and D. Wang, *J. Am. Chem. Soc.*, 2011, 133, 2398-2401.
18. K. Sivula, R. Zboril, F. Le Formal, R. Robert, A. Weidenkaff, J. Tucek, J. Frydrych and M. Grätzel, *J. Am. Chem. Soc.*, 2010, 132, 7436-7444.
19. R. Morrish, M. Rahman, J. M. D. MacElroy and C. A. Wolden, *ChemSusChem*, 2011, 4, 474-479.
20. P. Kumar, P. Sharma, R. Shrivastav, S. Dass and V. R. Satsangi, *Int. J. Hydrogen Energ.*, 2011, 36, 2777-2784.
21. S. Shen, P. Guo, D. A. Wheeler, J. Jiang, S. A. Lindley, C. X. Kronawitter, J. Z. Zhang, L. Guo and S. S. Mao, *Nanoscale*, 2013, 5, 9867-9874.
22. P. Liao, M. C. Toroker and E. A. Carter, *Nano Lett.*, 2011, 11, 1775-1781.
23. B. S. Yeo and A. T. Bell, *J. Phys. Chem. C*, 2012, 116, 8394-8400.
24. M. Dincă, Y. Surendranath and D. G. Nocera, *Proc. Natl. Acad. Sci.*, 2010, 107, 10337-10341.
25. Y.-F. Li and A. Selloni, *ACS Catal.*, 2014, 4, 1148-1153.
26. H. P. Klug and L. E. Alexander, *X-Ray Spectrom.*, 1975, 4, A18-A18.
27. D. S. Dalavi, R. S. Devan, R. S. Patil, Y.-R. Ma, M.-G. Kang, J.-H. Kim and P. S. Patil, *J. Mater. Chem. A*, 2013, 1, 1035-1039.
28. X. Meng, G. Qin, W. A. Goddard, S. Li, H. Pan, X. Wen, Y. Qin and L. Zuo, *J. Phys. Chem. C*, 2013, 117, 3779-3784.
29. L. Zhang, Y. Zhong, Z. He, J. Wang, J. Xu, J. Cai, N. Zhang, H. Zhou, H. Fan, H. Shao, J. Zhang and C.-n. Cao, *J. Mater. Chem. A*, 2013, 1, 4277-4285.
30. C. Du, X. Yang, M. T. Mayer, H. Hoyt, J. Xie, G. McMahon, G. Bischofing and D. Wang, *Angew. Chem. Int. Ed.*, 2013, 52, 12692-12695.
31. S. D. Tilley, M. Cornuz, K. Sivula and M. Grätzel, *Angew. Chem. Int. Ed.*, 2010, 49, 6405-6408.
32. T. Hisatomi, F. Le Formal, M. Cornuz, J. Brillet, N. Tetreault, K. Sivula and M. Gratzel, *Energy & Environ. Sci.*, 2011, 4, 2512-2515.

33. M. Barroso, A. J. Cowan, S. R. Pendlebury, M. Grätzel, D. R. Klug and J. R. Durrant, *J. Am. Chem. Soc.*, 2011, 133, 14868-14871.
34. L. Xi, P. D. Tran, S. Y. Chiam, P. S. Bassi, W. F. Mak, H. K. Mulmudi, S. K. Batabyal, J. Barber, J. S. C. Loo and L. H. Wong, *J. Phys. Chem. C*, 2012, 116, 13884-13889.
35. L. Xi, S. Y. Chiam, W. F. Mak, P. D. Tran, J. Barber, S. C. J. Loo and L. H. Wong, *Chem. Sci.*, 2013, 4, 164-169.
36. L. Badia-Bou, E. Mas-Marza, P. Rodenas, E. M. Barea, F. Fabregat-Santiago, S. Gimenez, E. Peris and J. Bisquert, *J. Phys. Chem. C*, 2013, 117, 3826-3833.
37. G. Wang, Y. Ling, X. Lu, T. Zhai, F. Qian, Y. Tong and Y. Li, *Nanoscale*, 2013, 5, 4129-4133.
38. M. Li, J. Deng, A. Pu, P. Zhang, H. Zhang, J. Gao, Y. Hao, J. Zhong and X. Sun, *J. Mater. Chem. A*, 2014, 2, 6727-6733.
39. D. Cao, W. Luo, J. Feng, X. Zhao, Z. Li and Z. Zou, *Energy & Environ. Sci.*, 2014, 7, 752-759.
40. O. Zandi and T. W. Hamann, *J. Phys. Chem. Lett.*, 2014, 5, 1522-1526.
41. J. Deng, X. Lv, J. Gao, A. Pu, M. Li, X. Sun and J. Zhong, *Energy & Environ. Sci.*, 2013, 6, 1965-1970.
42. K. Gelderman, L. Lee and S. W. Donne, *J. Chem. Educ.*, 2007, 84, 685.
43. R. De Gryse, W. P. Gomes, F. Cardon and J. Vennik, *J. Electrochem. Soc.*, 1975, 122, 711-712.
44. F. Cardon and W. P. Gomes, *J. Phys. D: Appl. Phys.*, 1978, 11, L63.